Nuclear Instruments and Methods in Physics Research A 1094 (2027) 172158

Contents lists available at ScienceDirect

Nuclear Inst. and Methods in Physics Research, A

journal homepage: www.elsevier.com/locate/nima

Full Length Article

High-flux CZT characterization using laser and X-ray induced Transient-Current Technique

Debora Magalhaes [a,b,*], Matthew C. Veale [c], Marie Ruat [d], Mohammadtaghi Hajheidari [a], Joern Schwandt [b], Erika Garutti [b], Heinz Graafsma [a,e]

[a] Deutsches Elektronen-Synchrotron DESY, Notkestr. 85, 22607 Hamburg, Germany
[b] Detector Development Group - Institute for Experimental Physics, University of Hamburg, Luruper Chaussee 149, 22761 Hamburg, Germany
[c] UKRI Science & Technology Facilities Council, Rutherford Appleton Laboratory, Harwell Campus, OX11 0QX Oxfordshire, United Kingdom
[d] Detector and Electronics Group - European Synchrotron Radiation Facility, 71, avenue des Martyrs, 38043 Grenoble, France
[e] Mid Sweden University, Holmgatan 10, 851 70 Sundsvall, Sweden

ARTICLE INFO

Keywords:
Transient Current Technique
Charge collection
Mobility
CZT
Electric-field profile
Time-of-flight measurement

ABSTRACT

High-flux CdZnTe sensors are promising candidates for detecting high energy photons at 4th generation synchrotron and free-electron laser experiments. Especially in the unique case of the MHz pulse rates of European XFEL, it is imperative that the sensor collects the full deposited charge in 120 ns or less, and that there is negligible residual charge or dynamic changes in the detector properties at high fluxes. In that context, the Transient Current Technique (TCT) was used to study HF-CZT planar sensors, to characterize the charge transport properties of the sensors for various applied bias voltages. Two different electrode technologies were compared: one planar sensor had platinum contacts on both sides, while the other had platinum cathode and titanium-gold anode. The sensors were tested in a TCT station with a pulsed 660 nm laser and also taken to the P07-EH1 beamline at Petra III during a pulsed operation mode of the storage ring; transients were collected for different positions in the sensors and different X-ray beam intensities at 87 keV. Both studied sensors showed remarkable uniformity, good electron transport properties and fast charge collection for electric field strengths above 2000 V/cm; the titanium/gold anode device showed evidence of significant bias-induced polarization at low field strengths, while localized excess leakage current effects were observed to be more significant in the device with both platinum electrodes.

1. Introduction

The advent of diffraction-limited synchrotron sources and X-ray Free Electron Lasers (XFELs) has pushed the frontiers of X-ray applications towards ever-higher photon energies and fluxes. These advancements require the development of detectors capable of operating reliably in such demanding environments. Among the available technologies, hybrid pixel detectors represent the current state of the art, wherein a semiconductor sensor is bonded pixel-by-pixel to an Application-Specific Integrated Circuit (ASIC). This modular design allows for independent optimization of the sensor and ASIC, enhancing versatility across diverse experimental requirements.

While silicon remains the default material for semiconductor sensors — owing to its mature fabrication processes and excellent charge transport properties — its quantum efficiency declines sharply for photon energies exceeding 18 keV. This limitation leads to degraded photon statistics and increased radiation exposure of the underlying ASIC, thereby reducing detector longevity. To mitigate these shortcomings, high-atomic-number (high-Z) materials with superior quantum efficiency in high photon energy regimes are required.

Within the room-temperature detector community, compound semiconductors such as chromium-doped gallium arsenide (GaAs:Cr) [1,2], cadmium telluride (CdTe) [3] and cadmium zinc telluride (CZT) [4] are widely adopted as high-Z alternatives. While these materials are well-suited to operation at higher energies, they also have some issues that must be considered. Especially in CdTe and CdZnTe, the large specific mass of holes means their mobility is over an order of magnitude lower than that of electrons [4]. Growth of these materials is also more challenging than elemental semiconductors like Si and Ge, resulting in the unintentional introduction of impurities and crystalline defects that can act as traps for the charge carriers. For these reasons, detector systems based on Cd(Zn)Te typically operate in an electron collection mode, ensuring good charge collection efficiency.

* Corresponding author at: Deutsches Elektronen-Synchrotron DESY, Notkestr. 85, 22607 Hamburg, Germany.
E-mail address: debora.magalhaes@desy.de (D. Magalhaes).

https://doi.org/10.1016/j.nima.2026.172158
Received 31 July 2026; Received in revised form 29 September 2026; Accepted 7 October 2026
Available online 15 October 2026
0168-9002/© 2026 The Authors. Published by Elsevier B.V. This is an open access article under the CC BY license (http://creativecommons.org/licenses/by/4.0/).
Open access funding enabled and organized by Projekt DEAL.

Table 1
Planar sensors tested in the LI-TCT setup and their characteristics. Contacts are described in pad/sensor/pixel order.

Sensor label	Contacts	Area	Thickness
S1	Pt/CZT/Pt	$7.6 \times 7.6\,mm^2$	1.5 mm
S2	Pt/CZT/Ti/Au + SU8	$7.6 \times 7.6\,mm^2$	2 mm

Despite collecting electrons, the poor transport of holes can still cause unwanted effects in these sensors. Excessive trapping of holes can lead to a build-up of space charge in the sensors at higher photon fluxes, leading to a degradation of the internal electric field and, in turn, the detector response - a phenomenon known as flux-induced polarization [5].

In 2016, the high-flux $Cd_{0.9}Zn_{0.1}Te$ (HF-CZT) [6] was introduced and subsequently characterized under various conditions and methodologies [7–10]. Owing to its improved hole transport properties, HF-CZT has emerged as one of the most promising candidates for high photon energy, high-flux detection. However, its performance in highly demanding time-resolved applications such as those requiring the MHz X-ray pulse repetition rates at the European XFEL remains unexplored.

Detector-grade CZT is a weakly compensated, semi-insulating material with an exceptionally low intrinsic carrier concentration. It has a polar nature from growth, and the natively p-type cadmium-terminated face is typically employed as the pixelated anode and bump-bonded to the ASIC, while the n-type tellurium-terminated face serves as the cathode [11]. Under reverse bias, detrapped charge carriers are swept away from the junctions and into the bulk, leaving behind fixed ionized acceptors (e.g. cadmium vacancies) or donors (e.g. tellurium antisites). This generates an opposing internal electric field that may weaken or even counteract the externally applied field. Such behavior, termed bias-induced polarization, is frequently observed in CdTe sensors with Schottky contacts [12]: while such contacts block the injection of charge carriers and result in devices with lower leakage current and better signal-to-noise performance, they effectively starve the detector from free charge carriers that could otherwise compensate the space charge arising from the biasing.

In this work, we present a comprehensive characterization of planar HF-CZT sensors with Schottky contacts, employing both laser-induced and X-ray-induced Transient Current Technique (TCT). The investigation aims to evaluate their suitability for integration into Adaptive Gain Integrating Pixel Detector (AGIPD) systems [13], with specific focus on their applicability to European XFEL experiments. Additionally, two distinct electrode technologies were comparatively assessed under identical experimental conditions.

2. Materials and methods

Planar sensors fabricated using proprietary Travelling Heater Method (THM) material growth and fabrication processes were provided by the Science and Technology Facilities Council (STFC-UKRI). Table 1 lists the two planar sensors covered in the scope of this work and their main characteristics. The metal contacts are described in [pad (Te-face)]/[sensor]/[pixel (Cd-face)] order.

One of the planar devices has platinum contacts deposited on both faces; the other has platinum pad (Te-face) and titanium-gold pixel (Cd-face), in a new electrode technology aiming at improving previously observed excess leakage current effects [10] and offering better mechanical properties for the sensor-to-ASIC assembly process. In addition, a epoxy-based polymer film (SU8) passivation layer was deposited on the gold electrode, with an opening of 1.80 mm × 3.8 mm at the center, as shown in Fig. 1. Both tested devices have 7.56 mm × 7.56 mm area. Sensor S1 represents the reference material sensor in this study, as pixelated devices of the same generation and electrode technology were bump-bonded to ASICs and tested in previous characterization campaigns [14].

The pad (Te-)faces of the sensors were glued with silver epoxy to the gold pads of dedicated PCBs. Wires for ground and bias voltage were glued to the gold pad and to the pixel (Cd-)face of the sensors respectively. The assembly was then mounted to a copper case also designed for this purpose. Both the board and the copper case were designed with a >2 mm opening in the sensor position, to allow irradiation of the sensors from both sides. Care was taken to avoid covering the opening with the silver glue.

2.1. Laser-induced TCT setup

The TCT setup has been used to determine effective trapping times and electric field distributions in irradiated silicon sensors since its installation in 2010 [15,16]. It allows the user to perform laser-induced TCT with less than 90 ps laser pulses of a few different selectable wavelengths (660 nm, 830 nm, 1015 nm and 1052 nm), using a Sepia II multi-channel Picosecond Diode Laser driver from PicoQuant [17]. The setup is shielded by a metal box to reduce electrical interference. Additionally, the laser is equipped with optics to focus the beam to 10 μm FWHM [16].

The detector stage has a motorized X-Y movement of minimum 50 nm steps with 20 nm precision. The laser stage can be adjusted in Z (direction of the laser) for changing the focus spot size on the detector, with 100 nm steps and 30 nm precision [16]. Additionally, the detector stage can be configured in two different positions, for top- or edge-irradiation of the sensor under study. Fig. 2 shows the setup inside the metal box, with a sensor mounted for top-TCT.

The sensors were biased by a Keithley 6517 A power supply, connected through a Bias-T to the pixel (Cd-)face of the sensors. The Bias-T is required to separate the DC level of the high-voltage bias from the transient signal coming from the sensor. The transient signal is transmitted to an amplifier; in this case, a Particulars AM-2 A 53 dB with a bandwidth of 0.01 MHz to 3000 MHz was used. The output of the amplifier is then connected to the high-sampling-rate oscilloscope (Rohde & Schwarz RTO2044, 20 GSa/s, 4 GHz), which was set to be triggered by the trigger output of the laser driver.

The bandgap energy of CZT can vary with the exact zinc concentration; in this work the reference value of 1.57 eV [4] for 10% zinc was adopted. The 660 nm laser was chosen for the experiment, to be above the bandgap and have a superficial depth of interaction (estimated optical penetration depth of 1 μm [18]). This is a necessary condition to have one charge carrier type inducing signal at a time, and characterize their transport properties individually. Time-dependent measurements were also done for a few bias voltages.

All measurements were conducted at room temperature. Although the temperature of the sensor was not actively monitored during the experiment, the laser pulse frequency was kept to a maximum of 160 Hz, giving enough time between pulses for the heat to be dissipated laterally on the sensor and the metal electrode. Therefore, local heating effects were considered negligible for the study.

2.2. X-ray TCT setup

The planar sensors were also tested with X-ray pulses during a beamtime at Petra-III beamline P07/EH1, while the storage ring was configured to 40-bunch mode (192 ns between bunches, equivalent to 5.2 MHz pulses). The 87 keV monochromatic beam was defined with the beamline slits to 100 μm × 100 μm. A TCT setup was used to collect the transients generated by each 44 ps RMS X-ray pulse [19]. This time, an ISEG SHR 20 60r power supply, an HSA-X-2-40 Femto amplifier of 40 dB and 2 GHz bandwidth, and a Tektronix MSO 4104 5GSa/s 1 GHz oscilloscope were used, keeping the same Bias-T; the more intense and more penetrating source required less amplification than the Laser-Induced TCT setup. The trigger for the acquisitions was defined by the full revolution bunch clock of the storage ring (130 kHz), so each acquired waveform contained 40 pulses, corresponding to the 40 electron bunches of each revolution.

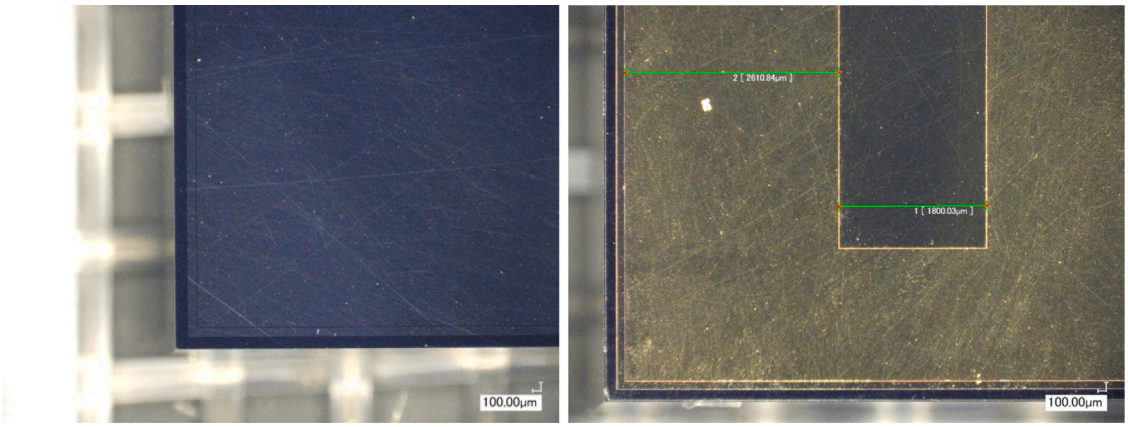


Fig. 1. Optical images of two planar sensors tested. Left: the anode side of sensor S1. Right: the anode side of sensor S2, with the passivation opening at the center.

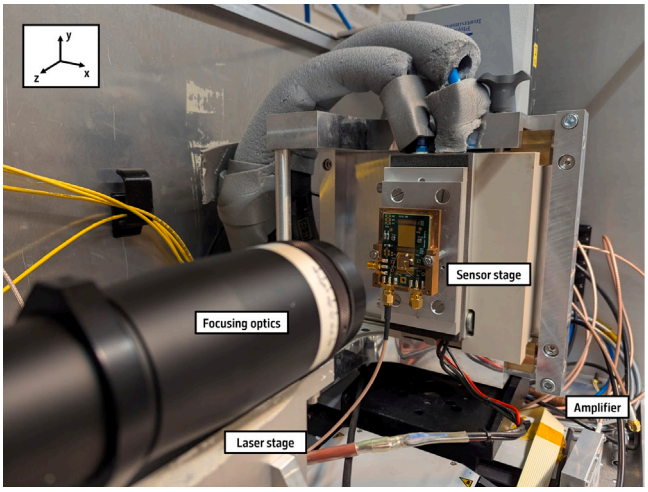


Fig. 2. LI-TCT setup inside the enclosure. The picture shows the focusing optics for the laser on top of the laser stage, the sensor under study mounted on the sensor stage, and the amplifier. The system coordinates are indicated on the top of the image.

The sensors were mounted on the sample stage as shown in Fig. 3(a). A 3D-printed plastic case was used instead of the copper case, to allow the beam to pass through and irradiate the pad side of the sensors with no limitation on the exposed area. The detector stage was scanned in front of the beam, mapping half the area of each sensor under study, as illustrated in Fig. 3(b); this scan was repeated for 4 different beam attenuation settings, covering intensities of 115 photons/pulse to 500 photons/pulse. A reverse bias voltage of 1000 V was applied to sensor S1 and 1333 V to sensor S2, for the same applied electric field strength of 6666 ± 1 V/cm.

The heat diffusion time estimated for a 100 µm×100 µm spot in CdTe is ≈2 ms, considering the thermal diffusivity of CdTe ($\alpha = 5.8 \times 10^{-6}$ m^2/s) [20]; the 5.2 MHz pulsed X-ray source is considered continuous from the thermal perspective. Even though the pulsed X-ray scenario is thermally more demanding than the pulsed laser, the calculated steady-state increase in temperature for the setup with 500 photons/pulse and equivalent power of 36.3 µW is 6.9 mK [21], and was neglected for this study.

3. Results and discussion

3.1. Laser-induced TCT

The transient current pulses induced by the 660 nm laser light when illuminating the pad side of sensor S1 under reverse bias are shown in Fig. 4(a), corrected for the impedance and amplification of the setup, for applied bias voltages of 350 to 1100 V. Thousands of waveforms were collected and averaged for each bias voltage. The transient signal can be integrated with Eq. (1) to generate a profile of the accumulated collected charge as a function of time, which is shown in Fig. 4(b).

$$Q(t) = \frac{1}{R \times G} \int_0^t V(t)dt, \tag{1}$$

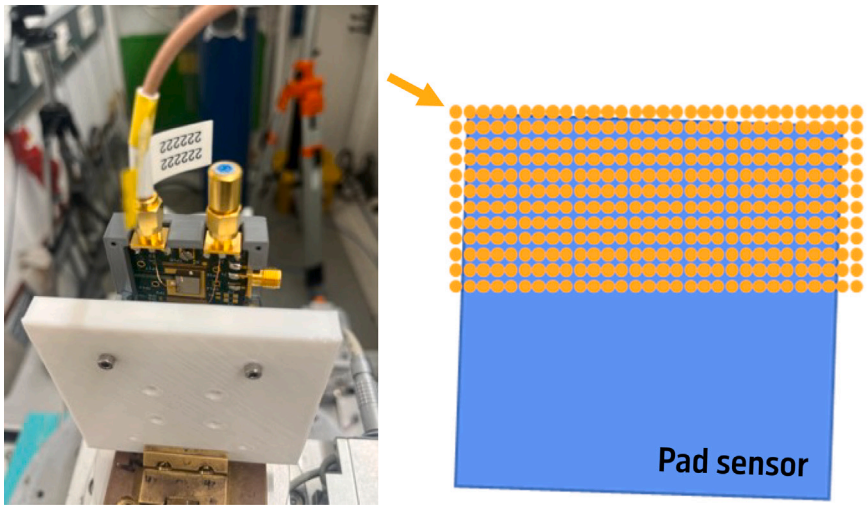
where R is the termination of the read-out channel of the oscilloscope (set to 50 Ω), G is the 53 dB amplification of the setup (factor 446.68), and V(t) is the oscilloscope-recorded transient signal.

Fig. 5 shows the same plots for sensor S2; the shape of the accumulated charge profiles are different to those in the S1, showing a non-linearity for lower bias voltages. In both sensors, small undershoots were observed after the transient current signals, and consequently a reduction in the total integrated charge can be observed after the maximum is reached. This undershoot was attributed to an impedance mismatch of the data acquisition setup, and the maximum value obtained for the charge was used as a metric for the analysis.

In this configuration, the laser light impinges on the platinum pads of the sensors, which are a few tens of nanometers thick [11]. The electrodes reflect the majority of the incident light (74.25%), while approximately 1.05% of the light is transmitted and reaches the CZT sensors [22]. The remaining 24.7% is absorbed by the metal. The laser power was set to the maximum, meaning an average optical power of 10 mW; 105 µW of which is deposited on the first micrometers of the sensors in less than 90 ps. According to previous calibration of the laser, this amounts to 0.32 pC per pulse, a similar amount to what has been reported in the literature [23].

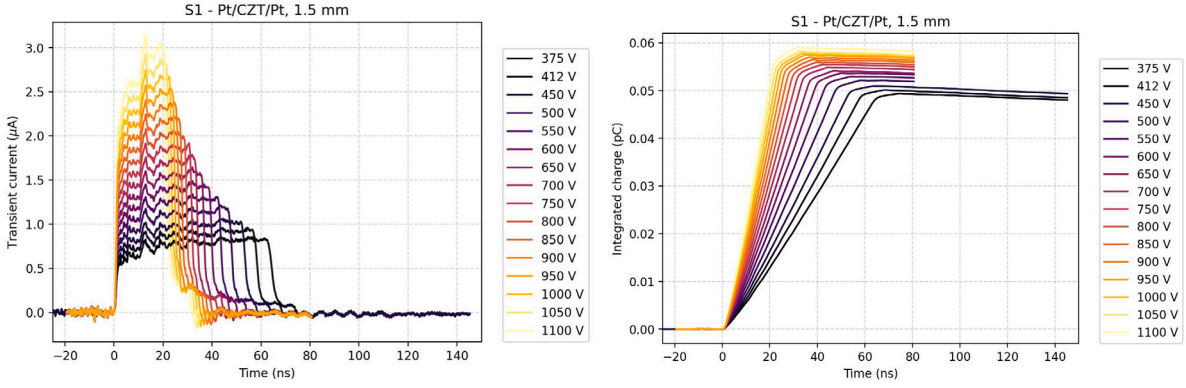
Under reverse bias condition, the pad electrodes acts as the cathodes, being negatively biased with respect to the pixel electrodes. The laser-generated electrons are drifted away from the pad and through the sensor thickness, inducing a current signal. The holes, on the other hand, drift a short distance towards the cathode and are immediately collected, so the measured induced current signals were dominated by moving electrons. Likewise, in forward bias condition the current signal generated by impinging the laser on the pixel side is induced mainly by electrons.

By obtaining the rise time of 10% to 90% of the integrated charge curve with a 100-points linear interpolation and multiplying it by 1.25,



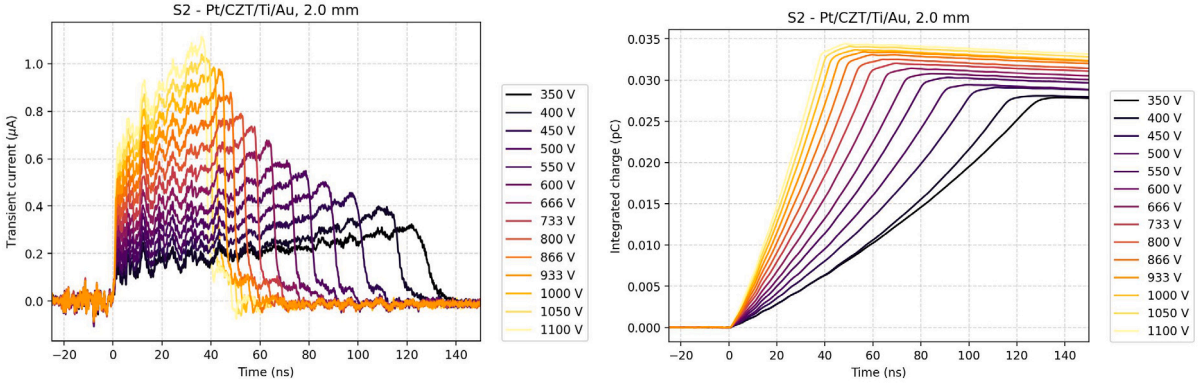
(a) (b)

Fig. 3. (a) Photo of a planar sensor installed at EH1 test facility from P07/Petra III. (b) Schematic of the 2D mapping of the CZT sensors; the tilted sensor illustrates the small misalignment of the sensors during the experiment.



(a) (b)

Fig. 4. (a) Transient current pulses obtained from the oscilloscope for sensor S1, applying positive bias voltages from 375 to 1100 V on the pixel side (reverse bias), and impinging the 660 nm laser on the pad side. (b) Cumulative integration of the current pulses on the left, providing the accumulated collected charge as a function of time. The drift time can be obtained from the 10% to 90% risetime of the charge curve.



(a) (b)

Fig. 5. (a) Transient current pulses obtained from the oscilloscope for sensor S2, applying positive bias voltages from 350 to 1100 V on the pixel side (reverse bias), and impinging the 660 nm laser on the pad side. (b) Cumulative integration of the current pulses on the left, providing the accumulated collected charge as a function of time. A bending of the charge curve can be observed for this sensor at the lower bias voltages.

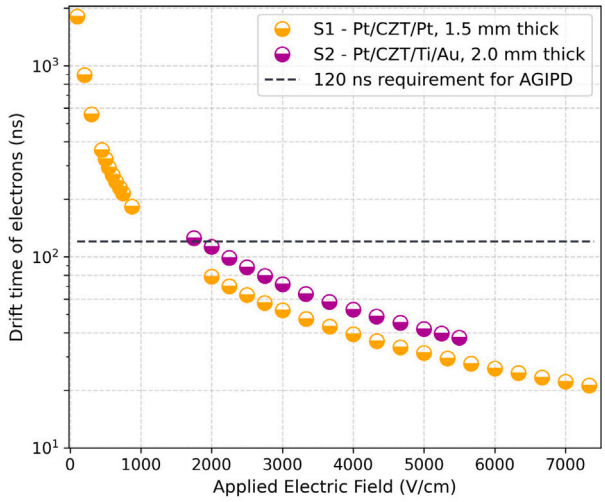


Fig. 6. Drift time of the electrons, obtained from the 10% to 90% risetime of the cumulative charge curves. The drift times fall beneath the 120 ns limit for applied electric fields higher than 2000 V/cm for both samples under reverse bias.

the total drift time of the electrons in each sensor can be obtained. Fig. 6 shows the total drift time as a function of the applied electric field (bias voltage normalized by the sensors thickness) for both sensors, with the dashed line marking the 120 ns acquisition time limit for 4.5 MHz operation with AGIPD. The drift times obtained for sensor S2 under similar electric field strength are understandably higher due to the ≈ 33% larger thickness. It can be observed that in both sensors the full charge of the laser pulse is collected faster than 120 ns for applied electric fields stronger than 2000 V cm^{-1}. For reference, the standard applied field during user operation is 5000 V cm^{-1}. This indicates that from the time-resolution perspective, the sensors are suitable for EuXFEL applications.

3.1.1. Time-dependent measurements

The current–voltage characteristics for each of the sensors (see Appendix A) demonstrated a clear Schottky-diode response, with sensor S2 being significantly more rectifying than S1. As with other materials like CdTe [24], the presence of a potential barrier at the metal–semiconductor junction means these devices are subject to bias-induced polarization. To characterize the evolution of such effect, time-resolved tests were performed with lower bias voltages for both sensors, collecting transients from the moment the bias voltage is powered on.

Fig. 7(a) shows the collected charge curves observed for sensor S1 over 15 min, reverse-biased at 60 V (400 V cm^{-1}). A subtle evolution with elapsed time can be observed: Fig. 7(b) shows plots of the maximum collected charge and average velocity ($v_{avg} = \frac{L}{t_{drift}}$) as a function of elapsed time. The maximum collected charge decayed to 91% of the initial value, and the average velocity decreased 2.9% during the experiment. The plots were fitted to exponential decay functions, and time constants of 71 ± 11 and 58 ± 15 s were extracted for the maximum charge and average velocity, respectively.

For sensor S2, a much more dramatic effect was observed in a shorter elapsed time, even for double the electric field strength. The History Mode from the oscilloscope [25] was used to save timestamps for individual waveforms over a shorter time scale. Fig. 8(a) shows the collected charge curves observed for sensor S2 over 160 s, reverse-biased at 200 V (1000 V cm^{-1}). Fig. 8(b) shows plots of the maximum collected charge and average velocity as a function of elapsed time. The maximum collected charge decayed to 85% of the initial value, and the velocity decreased 15% during the 162 s experiment; a further bending of the collected charge curve is observed. The plots were fitted to exponential decay functions and time constants of 26 ± 3 and 34 ± 3 s were extracted for the maximum charge and average velocity.

The fact that the S2 is highly rectifying indicates the presence of a larger potential barrier posed by the Ti/Au contact in comparison with the Pt contact; it follows that space charge generation is more likely, as there are less compensating holes being injected into the sensor. This can be seen clearly in the time-resolved measurements, with the net space charge in the sensor favoring bias-induced polarization.

The time-dependent analysis was repeated with sensor S2 for applied electric field strengths of 750, 1125, 1250, and 1375 V/cm. The measured values for charge and velocity after 60 s (Q_{60} and v_{60}, averaged from 60 to 65 s) compared to the initial values obtained for elapsed time = 0 (Q_0 and v_0, averaged from 0 to 5 s) were defined as the losses for each applied field. Fig. 9 shows such losses as percentages of the initial values of maximum charge ($100 \times \frac{(Q_0 - Q_{60})}{Q_0}$) and velocity ($100 \times \frac{(v_0 - v_{60})}{v_0}$), as a function of the applied electric field in sensor S2. It can be seen that the effect is reduced for stronger fields; by fitting the data points to exponential decay functions, the estimated loss for $E_{applied} = 5000$ V/cm is 0.009% in velocity and 0.007% in charge. The mitigation of the bias-induced polarization with higher applied field strengths is in agreement with previously reported results obtained for p-type CdTe [12,26].

3.1.2. Charge transport properties

With the drift times obtained from the transient signals at different applied bias voltages, it is possible to obtain an average velocity by assuming the charge path to be the entire thickness L of the fully depleted sensors, and the measured signal to be dominated by a single carrier. By evaluating how the average velocity v_{avg} evolves with the applied bias V, the mobility μ of the charge carriers can then be extracted by the slope of the average velocity plot as a function of the applied electric field (Eq. (2)).

$$v_{avg} = \frac{L}{t_{drift}} = \mu \times \frac{V}{L} = \mu \times E_{applied} \tag{2}$$

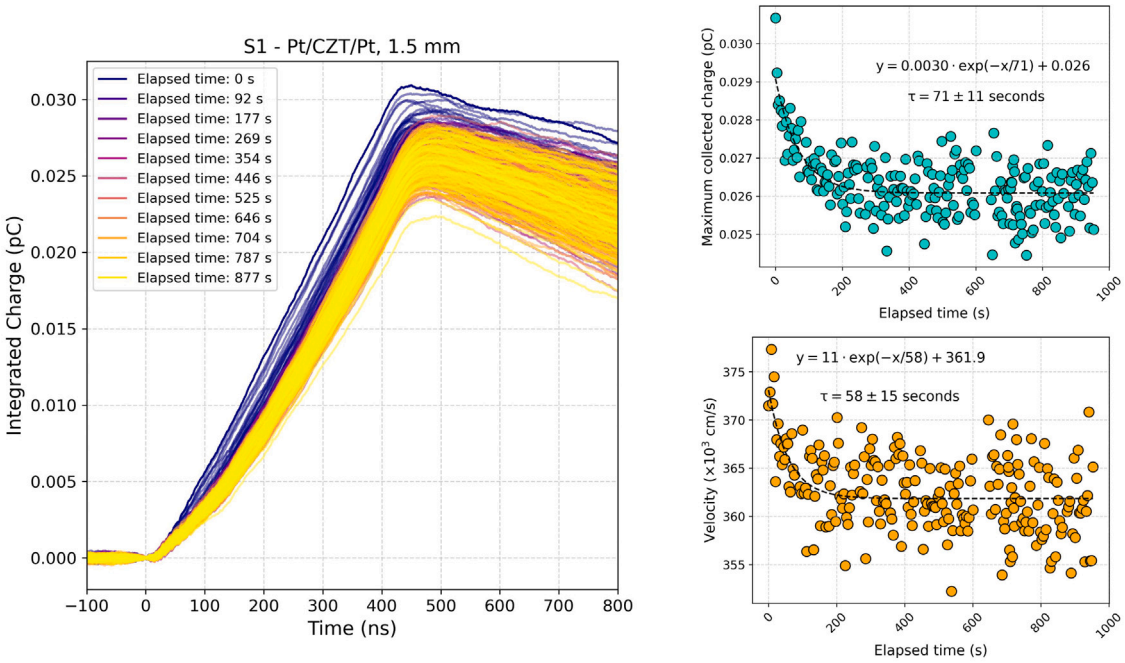
Fig. 10 shows the average velocity plot obtained for electrons drifting through S1 and S2 under reverse bias. The data are plotted as a function of the applied electric field $E_{applied}$ for a more straightforward comparison of the devices. Electron mobility values of $\mu_e = 964 \pm 1$ cm^2 V^{-1} s^{-1} and $\mu_e = 1002 \pm 2$ cm^2 V^{-1} s^{-1} were obtained, respectively. The linear coefficient obtained is associated with a minimum electric field to induce signal (E_{min}), and was considered negligible.

Furthermore, the $\mu\tau$ products defining the charge transport properties in semiconductor sensors, with τ being the lifetime of the charge carriers, are usually obtained by fitting a plot of the total collected charge as a function of the applied bias voltage to the single-carrier Hecht equation [1,7], which is applicable in this case.

Eq. (3) was used to fit the maximum collected charge obtained from each sensor as a function of the applied bias voltage, including a velocity parameter S [24,27] to account for surface recombination effects. The fit was applied to data obtained collecting electrons in forward bias configuration, to minimize non-uniformities of the electric field associated with bias-induced polarization; for electron collection, this means irradiating the pixel side of each sensor, while applying a negative bias voltage to the same electrode.

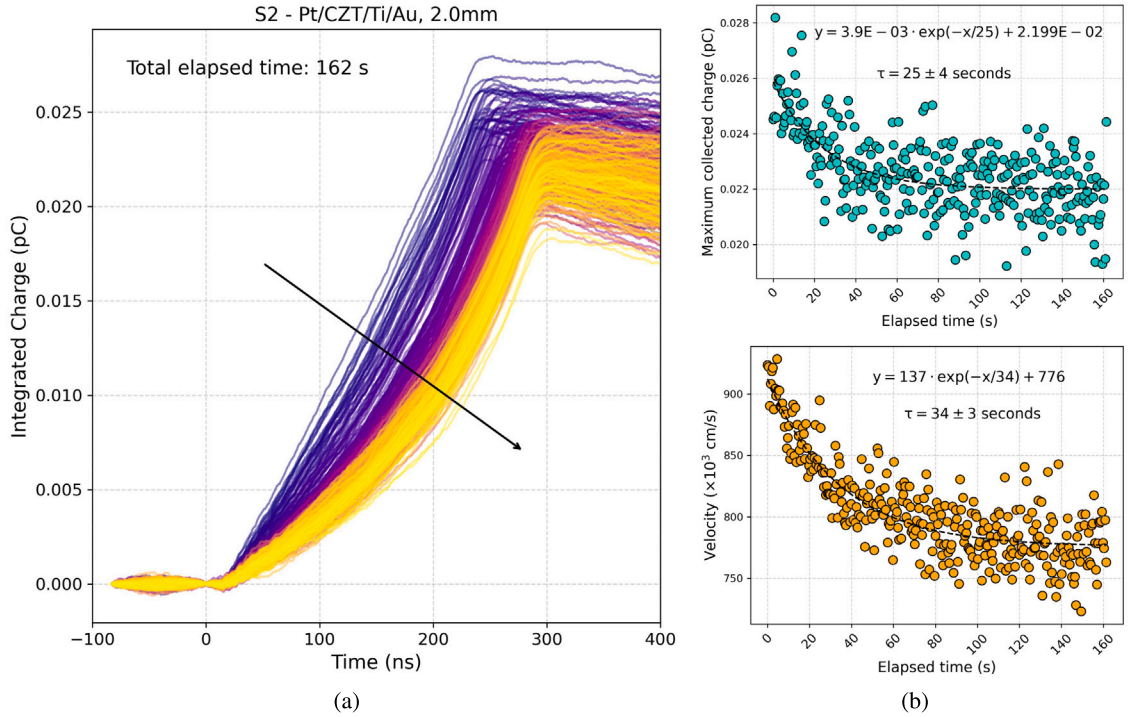
$$Q = Q_0 \times \frac{\mu_e \tau_e V}{L^2}\left[1 - exp\left(-\frac{L^2}{\mu_e \tau_e V}\right)\right] \times \left(\frac{1}{1 + L \times S/\mu_e V}\right) \tag{3}$$

In Eq. (3), Q_0 is the total deposited charge in the sensor, $\mu_e\tau_e$ are the mobility and lifetime figures for electrons, V is the applied bias voltage, L is the sensor thickness and S is the surface recombination velocity. The collected charge data as a function of the forward applied electric field $E_{applied}$ and the corresponding fits to the modified Hecht Eq. (3), with Q_0, S and $\mu_e\tau_e$ as free parameters, are shown in Fig. 11 for both sensors.



(a) (b)

Fig. 7. Evolution in time of the cumulative charge curves obtained for sensor S1, for an applied reverse bias voltage of 60 V (400 V/cm) and for a time interval of 1000 s. A small decay of the maximum collected charge can be observed. (b) The maximum charge and the average velocity were plotted as a function of the elapsed time: by fitting the data points to exponential functions, time constants of 71 ± 11 and 58 ± 15 s were obtained for the charge and the velocity, respectively.



(a) (b)

Fig. 8. Evolution of the cumulative charge curve obtained for sensor S2, for an applied reverse bias voltage of 200 V (1000 V/cm) and for a time interval of 162 s. The arrow direction indicates the elapsed time evolution. A decay of the maximum collected charge and an increasing bending of the curves can be observed. (b) The maximum charge values and the average velocities were plotted as a function of the elapsed time: by fitting the data points to exponential functions, time constants of 26 ± 3 and 34 ± 3 s can be obtained for the charge and the velocity, respectively.

A reasonable fit was obtained for sensor S1, with $\mu_e\tau_e = 1.7 \pm 0.3 \times 10^{-3}$ cm^2 V^{-1} and $S = 2.7 \pm 0.1 \times 10^5$ cm s^{-1}. Using the μ_e value obtained with Eq. (2), these result in $\tau_{e,bulk} = \mu_e\tau_e/\mu_e = 1.8 \pm 0.3$ µs and $\tau_{e,surface} = L/S = 0.56 \pm 0.02$ µs. For sensor S2, a regime transition was observed when the forward bias voltage surpassed 160 V, deviating the collected charge from the predicted behavior. The data points obtained

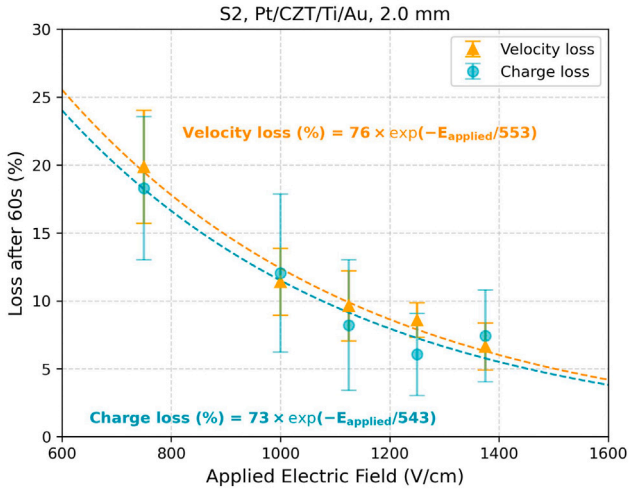


Fig. 9. Percentage of losses in charge and velocity after 60 s for different bias voltages, averaging for 5 s. The effect is reduced for stronger applied electric field. Exponential decay functions were fitted to the datapoints to illustrate the trend.

for lower voltages did not provide enough statistics to disentangle the surface effect from the bulk characteristics. By fixing the bulk lifetime to match the value obtained for S1, a surface recombination velocity of $S = 0.60 \pm 0.03 \times 10^5$ cm s^{-1} is obtained, corresponding to $\tau_{e,surface} = 3.3 \pm 0.2$ µs.

While the sensors are expected to have similar bulk characteristics, their irradiated surfaces are significantly different; the irradiated electrode in S1 is made of platinum, while in S2 is titanium/gold. This difference can be identified when comparing the surface lifetime ($\tau_{e,surface}$) values for electrons obtained for each sensor: the titanium/gold electrode presented a surface lifetime 6× longer than the platinum electrode.

3.1.3. Electric field profiles

Different approaches to extract information on the electric field from the transients are explored in the literature [28–31]. The main challenge for High-Z sensors is that the electric field in these sensors cannot be assumed to be uniform; effects like bias-induced polarization and charge trapping are likely to occur and influence the electric field profile. The approach introduced by Uxa et al. [30] was the method chosen for this analysis. It assumes the space charge density for a given bias voltage was in the stable regime during the data acquisition, and that the electric field profile affected by such space charge density is linear.

Eq. (4) was used to fit the transient current signals $I(t)$ obtained under reverse-bias conditions, and extract the electric field slope a and the field immediately under the pad E_{min}. The assumed values for μ and τ are the figures obtained in Section 3.1.2; L is the full thickness of the sensors, and Q_0 is the maximum charge collected by each sensor at the highest bias voltage. More details on the method and examples of transient signals and corresponding fits are presented in Appendix B.

$$I(t) = \frac{Q_0 \times \mu E_{min} \times e^{-(a+\frac{1}{\mu\tau})\mu t}}{L} \tag{4}$$

The resulting electric field profile when in user operation conditions ($E_{applied}$ of 5 kV cm^{-1}) is shown in Fig. 12(a). A rising slope can be observed for both sensors, with a weaker field region formed under the pad.

Space charge density values can then be obtained from the electric field slope using Eq. (5). The gradient of the space-charge affected electric field opposes the direction of the applied field; this means that negative space charge is formed, and it can be seen in Fig. 12(b) that it increases with voltage. Moreover, sensor S2 shows higher space charge density values for the same applied electric field conditions.

$$\rho = \frac{\epsilon_0 \epsilon_s}{e} \times \frac{dE}{dx} \tag{5}$$

In Eq. (5), ρ is the space charge density in cm^{-3}, ϵ_0 is the vacuum permittivity, ϵ_s is the relative dielectric constant for CZT (10.9), and $\frac{dE}{dx}$ is the electric field gradient over the sensor thickness, given by the slope a.

3.1.4. Discussion of the LI-TCT results

It has been reported that the main source of leakage current in HF-CZT under reverse bias conditions comes from injection of positive charge carriers into the Cd-face, from the anode through a ≈10 nm thick $CdTeO_3$ interfacial layer [11,32,33].

According to the literature [32], the oxide layer pins the Fermi level in the middle of the CZT bandgap, producing a fixed barrier height in the order of 0.76 eV to 0.79 eV for platinum contacts that has been experimentally measured. The titanium anode, however, would form a barrier for electrons of $\phi_e = \phi_{Ti} - \chi = 4.33 - 4.3 = 0.03$ eV and hence a barrier for holes of $\phi_h = E_{BG} - \phi_e = 1.57 - 0.03 = 1.54$ eV, being ϕ_{Ti} the titanium work function, χ the CZT electron affinity and E_{BG} the CZT bandgap.

The disparity in barrier heights fundamentally dictates the operational differences observed in this Section between the two devices. While the relatively low ≈0.77 eV barrier of Pt allows partial hole injection to neutralize the ionized acceptors close to the anode, the substantially higher 1.54 eV barrier of Ti/Au effectively blocks hole injection entirely. This phenomenon results in more negative space charge near the anode, and a sensor comparatively more prone to bias-induced polarization, as has been observed in Section 3.1.1 for the time-dependent measurements at lower bias voltages and confirmed by the electric field profiles and space charge densities obtained in Section 3.1.3. However, it is expected to have a small or negligible impact for sufficiently high applied electric field strengths.

On the other hand, the very low, *quasi*-ohmic Ti/Au barrier for electrons in forward bias operation leads sensor S2 to quickly reach the space charge limited current (SCLC) regime, being overflown with charge carriers more rapidly than sensor S1, where a significant barrier of $\phi_e = \phi_{Pt} - \chi = 5.65 - 4.3 = 1.35$ eV still exists. The regime transition around 160 V = 800 V/cm observed in Fig. 11 can also be identified in S2 current–voltage characteristics (Appendix A).

The mobility and lifetime values obtained for electrons are within the range of the literature reported values for HF-CZT obtained with alpha particles [34]. However, a similar analysis of the hole transport properties could not be performed. This is related to limitations of the laser-induced TCT method: the very superficial (≈1 µm [18]) generation of charge carriers makes them more susceptible to surface recombination effects and trapping on the highly defective interface region, especially for holes, known to be significantly less mobile. Moreover, to obtain a detectable signal from the holes in forward bias condition, very high bias voltages would be required; this was not possible with sensor S2 due to its very high leakage current.

For a better understanding of the sensors response at the final user application, the X-ray TCT is a more representative technique: the attenuation length for the 87 keV photons on CZT is expected to be 785.34 µm [35], therefore less susceptible to surface effects.

3.2. 2D mapping with X-ray TCT

Ten full revolutions of the electron bunches in the storage ring were recorded at each position of the scan, meaning 10 × 40 pulses were recorded and averaged, for a fixed electric field strength of 6666 ± 1 V/cm. Signal reflections due to impedance mismatch were identified in the raw signals, but could not be eliminated experimentally and were removed in data post-processing. The processed current pulses

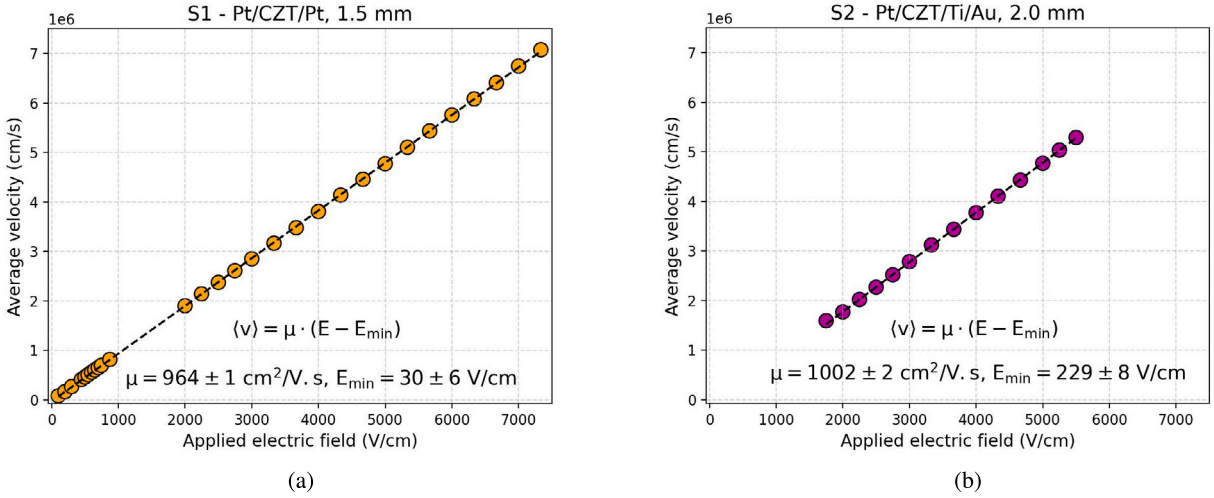


Fig. 10. Calculated average velocity ($v_{avg} = \frac{L}{t_{drift}}$) as a function of the applied electric field ($E_{applied}$) for electrons, in (a) S1 and (b) S2. From the slope of the plot, the charge carrier mobilities can be obtained. The linear coefficients corresponding to the minimum electric field to induce signal E_{min} were considered negligible for the rest of the analysis.

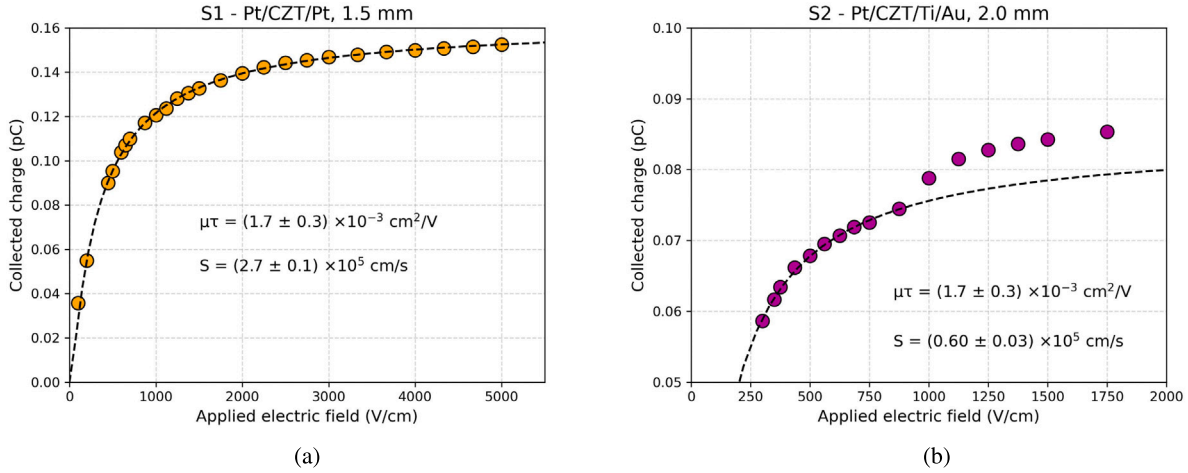


Fig. 11. (a) Maximum collected charge as a function of the applied electric field $E_{applied}$ for sensor S1 under forward bias. A reasonable fit to the single-carrier Hecht equation modified to include the surface recombination contribution was obtained, with a $\mu\tau$ value of $1.7 \pm 0.3 \times 10^{-3}$ cm^2 V^{-1}. (b) Measured collected charge as a function of the applied bias voltage for sensor S2 under forward bias. After the transition to space-charge limited current regime at ≈160 V, corresponding to 800 V cm^{-1}, the total collected charge metric deviates from the expected behavior. The remaining data points do not provide enough statistics for disentangling surface recombination effects and the electrons lifetime.

were integrated to charge as done in Section 3.1; the maximum charge collected per position of the beam in the sensor was mapped and is shown in Fig. 13 for both sensors. The charge collection times were also obtained from the integrated charge profiles, mapped and plotted as a function of the beam position in the sensors, and are shown in Fig. 13. A few regions were identified with aberrational behavior in both sensors and are marked in Fig. 13. Their behavior was reproducible for the four different beam intensities evaluated.

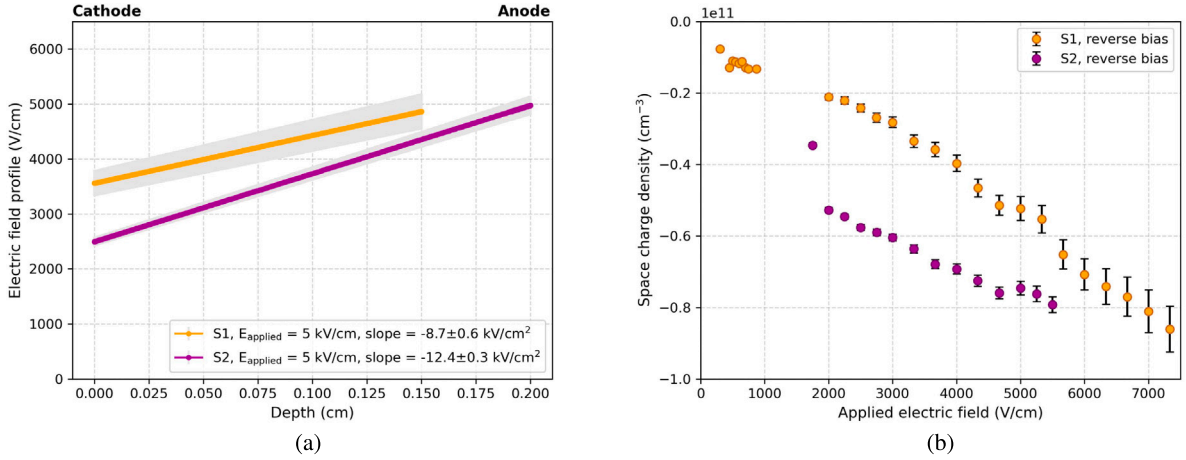
Examples of current pulses obtained for the marked region R2 are shown in Fig. 14(a). The current pulse obtained at position (2.5,3.0) has less amplitude than the ones obtained at neighboring positions and presents a bump after the falling edge, nevertheless resulting in the same total integrated charge as the other regions of the sensor.

The positions standing out in regions R1 and R3 in the charge maps show higher total integrated charge. A temporary shift of the pulse baseline can be observed in Fig. 14(b) for the S1 aberrant region R1 and in Fig. 14(c) for the S2 aberrant region R3, lasting almost 180 ns.

When it comes to AGIPD operation, the measured quantity is the integrated charge; even though the full photo-generated charge is collected within the 120 ns acquisition window, the remaining spurious charge arriving at the amplifier after 120 ns could impact the ASIC performance. If charge injection occurs during the reset phase of the electronics, it would generate a shift of the baseline in the next frame due to a misinterpretation of the dark signal. The collected charge can be extracted by the cumulative sum of the current transients and are shown in Fig. 15 for regions R1 and R3, from sensor S1 and S2 respectively. The inset plots show the excess charge accumulated after the 120 ns threshold in each sensor; it can be seen that sensor S1 shows an excess charge reaching 0.15 pC after the time threshold, while sensor S2 shows an excess charge after threshold in the same order of magnitude of the undershoot of the transients (negative slopes observed for the neighbor positions) and therefore considered negligible. In both sensors, the charge seems to reach a plateau before 170 ns, and no impact was observed in the subsequent pulses.

3.2.1. Discussion of X-ray TCT results

In the conditions of this experiment, both holes and electrons contribute to the signal formation; however, taking into account the electric field profile obtained in Section 3.1.3, the X-ray mass attenuation



(a) (b)

Fig. 12. (a) Electric field profiles obtained when applying a reverse bias voltage corresponding to $E_{applied} = 5\,\mathrm{kV\,cm^{-1}}$ for both sensors. A rising slope can be observed, with a lower field region beneath the pad. The gray shadow represent the error associated with the fitting. (b) Space charge density values obtained from the electric field slope for both sensors as a function of the applied electric field $E_{applied}$: a negative space charge is formed and increases with reverse bias voltage. Sensor S2 shows higher space charge density numbers for the same applied electric field.

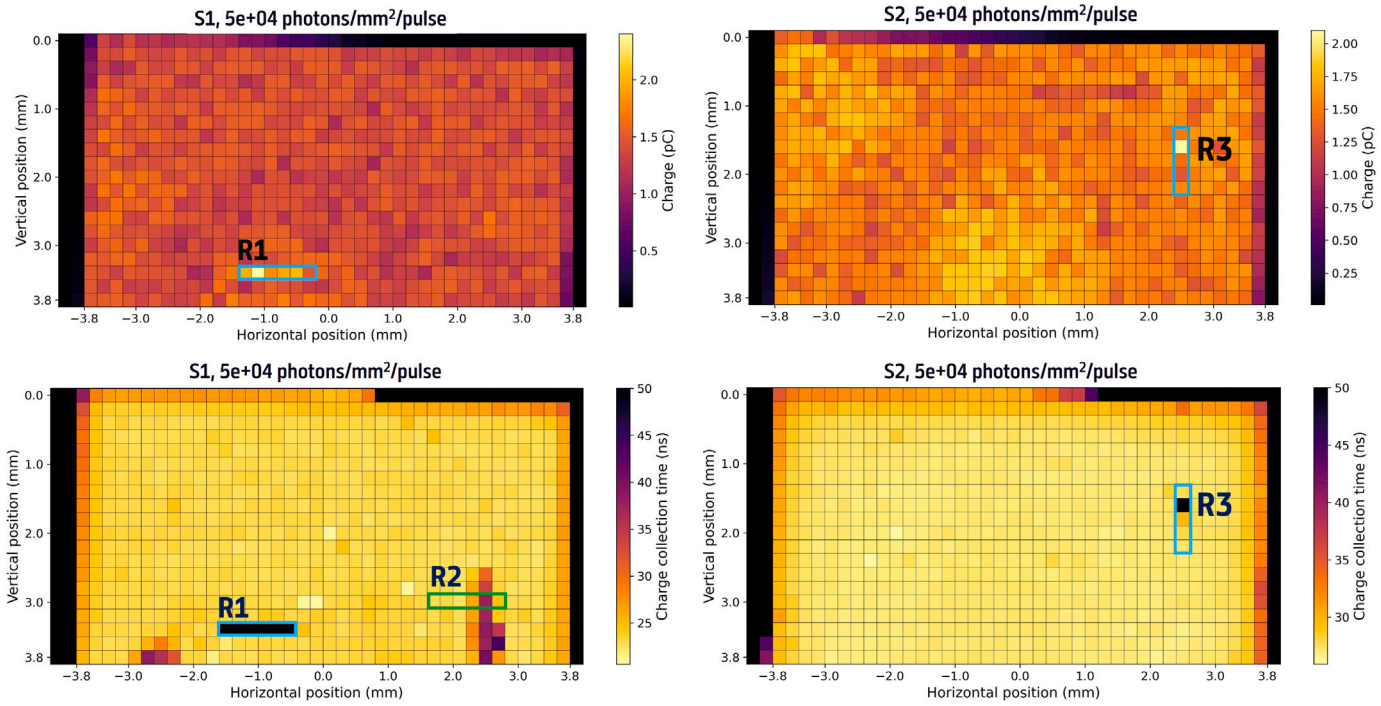
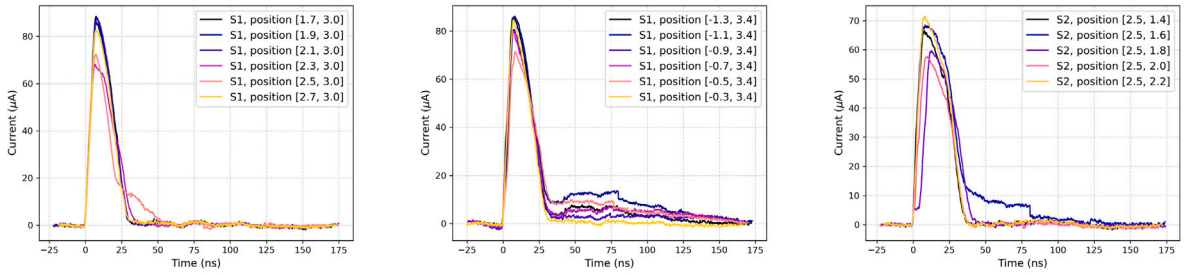


Fig. 13. Top: map of the collected charge per beam position on the S1 and S2 sensor areas. Bottom: map of the charge collection time per beam position on the S1 and S2 sensor areas. Regions with aberrational behavior and neighbors are marked as R1, R2 and R3. The applied electric field strength was 6666 ± 1 V/cm for both sensors.

coefficient on CZT [35], the electron transport properties obtained in Section 3.1.2, and the most recent hole transport properties reported for a similar sensor [34], the integrated charge contribution of holes would account for 18.8% in the 192 ns window between pulses. Therefore, the analysis was performed considering only the major contribution of electrons to the signal.

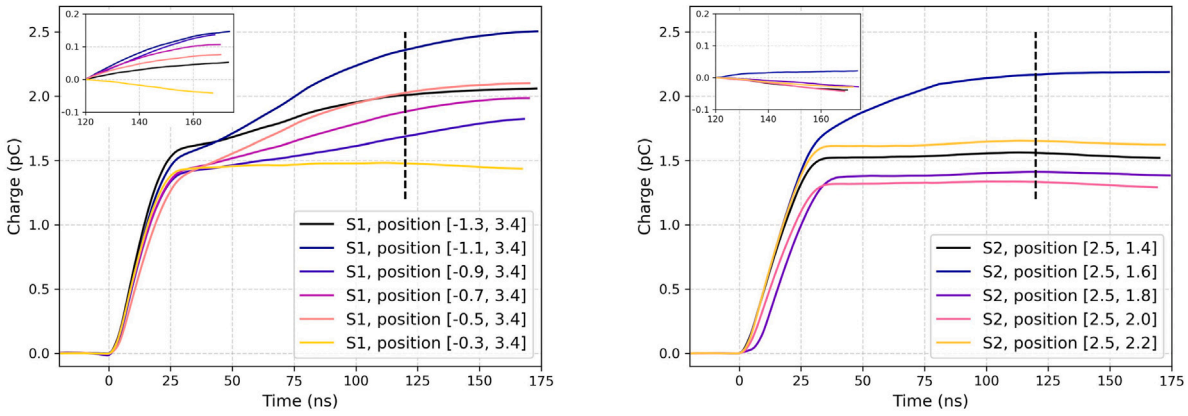
The effect observed in Fig. 14(a) can be intuitively associated with a partial amount of trapped charges (electrons) arriving later to the electrode, likely related to sensor defects at this position in the sensor. On the other hand, the excess of charge observed in Figs. 14(b) and 14(c) can only be explained by a highly-localized excess-leakage current effect, in a similar fashion to what has been observed by Cline et al. [10]: the nature of the electrodes change temporarily from blocking to injecting charge carriers, due to a build-up of trapped charge at the interface layer that effectively reduces the potential barrier height. However, this effect was not yet characterized for such high instantaneous photon intensities as the ones reached in this experiment, with an estimated flux of 5×10^4 87 keV photons/mm^2/pulse for pulses of 44 ps RMS [19].

This effect could have an impact on the ASIC operation of these sensors at 4.5 MHz in EuXFEL, since it lasts longer than the 120 ns acquisition time limit. However, besides being highly localized, the accumulated charge for 55 ns after the acquisition window of 120 ns is below 0.2 pC for S1 and below 0.05 pC for S2 for all evaluated pulses. The charge was observed to stabilize at ≈170 ns, and no impact was observed on the subsequent pulses during the 5.2 MHz bunch-rate



(a) (b) (c)

Fig. 14. Examples of transients for the marked regions in Fig. 13. (a) Transients of the region R2 in sensor S1: the longer charge collection time seen for position (2.5,3.0) is associated with the late arrival of trapped charges. (b) Transients of the region R1 in sensor S1: the longer charge collection times are associated with an excess of charge in those positions, which last longer than the pulses. This effect is compatible with the "Excess leakage current" phenomenon described by Cline et al. [10]. (c) A similar excess leakage current effect is observed for region R3 in sensor S2.



(a) (b)

Fig. 15. Accumulated collected charge as a function of time (a) at region R1 of sensor S1 and (b) at region R3 of sensor S2. The black dashed line marks the end of the acquisition window at 120 ns, while the inset plots show the excess charge accumulated after the mark. It can be seen that in sensor S1 the charge continues to increase after the acquisition window, before reaching a plateau at ≈170 ns.

operation. It must be noted that sensor S2 shows a significantly better performance in that regard, leading to the conclusion that there was indeed an improvement on the impact of the Excess Leakage Current effect on the data with the new Ti/Au electrode technology.

4. Conclusion and future prospects

The charge transport properties of electrons on CZT sensors were successfully characterized using laser-induced TCT. The drift time of electrons was evaluated for different bias voltages and for the two electrode technologies, and has proven to be conclusively fast enough for 4.5 MHz operation with AGIPD when in user conditions of biasing (5000 V/cm).

The electric field profiles inside the sensors were evaluated and a model was proposed to explain their behavior. Bias-induced polarization was observed in both sensors during time-dependent measurements, being significantly stronger for the Ti/Au electrode device; a bias refresh is recommended for user operation of the detector over longer (> 12 h) time scales.

The mobility and lifetime of electrons drifting through the sensors were evaluated under forward bias using a modified Hecht equation to account for surface recombination effects, and the obtained figures are compatible with results for this sensor material reported in the literature [34]. The transport properties of holes could not be explored due to experiment limitations.

The planar sensors were also tested under high intensity 87 keV X-ray pulses; overall a high uniformity of the response was observed over the sensors areas, both in terms of charge collection and drift time. For the few regions with abnormal behavior, the excess charge after 120 ns was below 0.2 pC (14% of the average photo-generated charge) for the device with platinum contacts, and below 0.05 pC (3.6% of the average photo-generated charge) for the device with Ti/Au anode. In both cases, the excess charge is stable after 170 ns and no interference between pulses was observed. Furthermore, their functionality was not impacted by the high fluxes used (equivalent to 2.6×10^{11} photons/mm^2/s), implying that no flux-induced polarization was observed for these sensors in the evaluated flux range.

In view of the aspects covered by this study, the material is considered suitable for high frame-rate operation at XFELs. While the Ti/Au electrode seems to have successfully mitigated the Excess Leakage Current effect, being more suitable for spectroscopic applications, the standard Pt electrode presented higher stability in terms of bias-induced polarization and would be more suitable for long-term operation. Meanwhile, further experiments with pulsed X-ray illumination of pixelated devices bump-bonded to AGIPD ASICs are planned for the near future, where the sensor material will be put to test under application conditions.

CRediT authorship contribution statement

Debora Magalhaes: Writing – original draft, Visualization, Software, Project administration, Methodology, Investigation, Funding acquisition, Formal analysis, Data curation, Conceptualization. **Matthew**

C. Veale: Writing – review & editing, Validation, Supervision, Resources, Methodology, Investigation, Funding acquisition, Data curation, Conceptualization. **Marie Ruat:** Validation, Software, Methodology, Investigation, Data curation, Conceptualization. **Mohammadtaghi Hajheidari:** Writing – review & editing, Validation, Investigation. **Joern Schwandt:** Validation, Software, Resources, Conceptualization. **Erika Garutti:** Writing – review & editing, Validation, Supervision, Resources, Conceptualization. **Heinz Graafsma:** Writing – review & editing, Validation, Supervision, Resources, Funding acquisition, Conceptualization.

Declaration of generative AI and AI-assisted technologies in the manuscript preparation process

During the preparation of this work, the author(s) used ChatGPT in order to improve the clarity of the text in Section 1 (Introduction). After using this tool/service, the author(s) reviewed and edited the content as needed and take(s) full responsibility for the content of the published article.

Declaration of competing interest

The authors declare that they have no known competing financial interests or personal relationships that could have appeared to influence the work reported in this paper.

Acknowledgments

The authors acknowledge the support of the STFC Centre for Instrumentation's Sensor Materials for Advanced Radiation Technologies (SMART) Managed Programme 2024–2026; of the "Stephenson Distinguished Visitor Programme" at DESY, which funded the visit of M. C. Veale in June 2025, and of the "PIER Short Visits" programme at DESY which funded the visit of M. Ruat for the beamtime in November 2025. We acknowledge DESY (Hamburg, Germany), a member of the Helmholtz Association HGF, for the provision of experimental facilities. Parts of this research were carried out at Petra III. Data was collected using the P07-EH1 in-house test facility operated by Helmholtz-Zentrum Hereon. We would like to thank Norbert Schell, Andre Rothkirch and Olof Gutowski for their assistance during the experiments. Beamtime was allocated for proposal "Hereon in-house H-20010018".

Appendix A. Current–voltage characteristics

The current–voltage characteristics of the two sensors were also characterized and are shown in Fig. 16. The bias supply is connected to the [pixel (Cd-)] face, meaning a negative bias voltage corresponds to forward bias, while a positive bias voltage corresponds to reverse bias.

The behavior of sensor S1 at forward bias show a transition from the linear regime ($I \propto V^{0.96\pm0.04}$) to space-charge limited current (SCLC) regime ($I \propto V^{1.86\pm0.02}$) at 263 V. Sensor S2 shows a transition from the linear/trap-filling regime ($I \propto V^{1.33\pm0.01}$) to SCLC regime ($I \propto V^{2.14\pm0.07}$) at 160 V, confirming what was observed in Fig. 11(b). Both sensors presented a rectifying behavior typical for Schottky contact sensors.

Appendix B. Method for obtaining the electric field profiles

The method presented by Uxa et al. was adapted to a negative slope a and a minimum electric field strength under the cathode E_{min} as follows. Assuming a linearly increasing electric field:

$$E(x) = E_{min} - a \cdot x \longrightarrow v = \frac{dx}{dt} = \mu(E_{min} - a \cdot x)$$

$$\int_0^x \frac{1}{E_{min} - a \cdot x} dx = \int_0^t \mu dt$$

$$\left.\begin{aligned} E(t) &= E_{min} \times e^{-a\mu t} \\ Q(t) &= Q_0 e^{-t/\tau} \end{aligned}\right\} \quad I(t) = \frac{Q(t)v(t)}{L} = \frac{Q_0\mu}{L} E_{min} \cdot e^{-(a+\frac{1}{\mu\tau})\mu t} = I_0 e^{-(a+\frac{1}{\mu\tau})\mu t} \tag{6}$$

Eq. (6) was used to fit the transient current signals, with I_0 and a as free parameters. Values of μ_e and τ_e obtained in Section 3.1.2 for each sensor were fixed as μ and τ. E_{min} was then obtained as $I_0 \times \frac{L}{\mu Q_0}$ using the maximum charge collected by each sensor at the highest applied bias voltage as Q_0.

Fig. 17 shows a few examples of transients obtained for sensors S1 and S2 and their respective fits.

Data availability

Data will be made available on request.

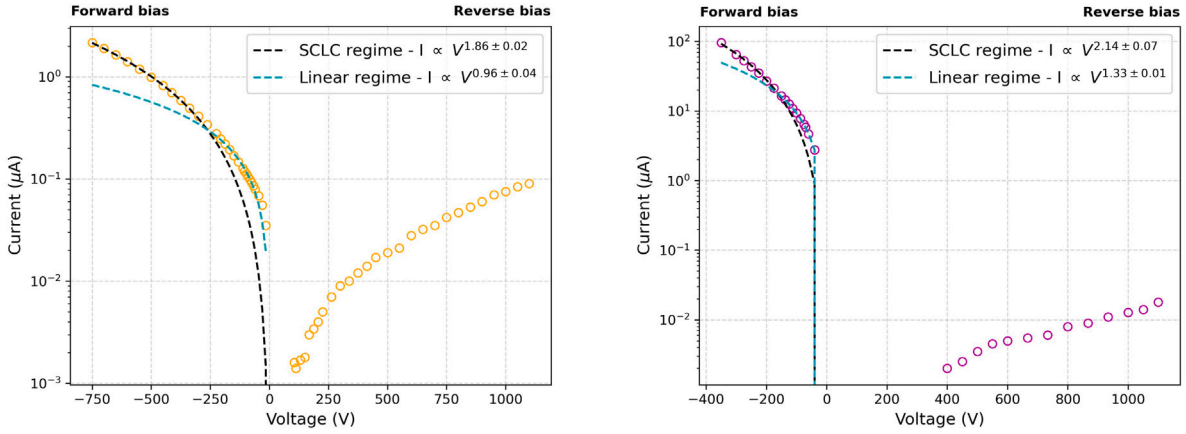


Fig. 16. (a) Current–voltage characteristics obtained for sensor S1, showing the absolute values of leakage current as a function of the bias voltage in a semi-log plot. As the bias voltage is applied to the pixel (Cd-) face, negative values correspond to forward bias, while positive values correspond to reverse bias regime. A transition from the linear regime to space-charge limited current (SCLC) regime in the forward bias can be observed at −263 V. (b) Current–voltage characteristics obtained for sensor S2; a similar transition from the linear/trap-filling regime to space-charge limited regime in the forward bias can be observed at −160 V.

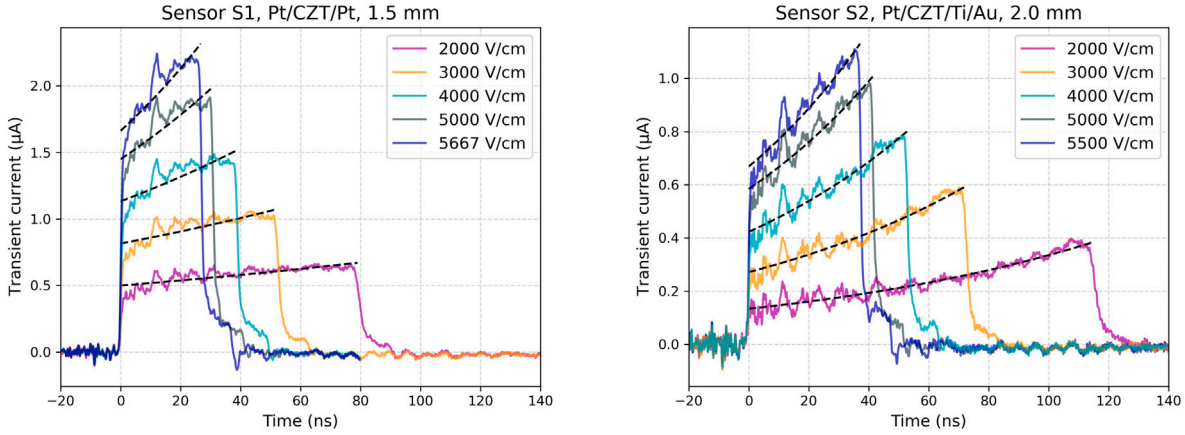


Fig. 17. Examples of current transients obtained for sensors S1 and S2 and their corresponding fits to Eq. (6) in dashed black. From the fits, the electric field under the cathode E_{min} and the electric field slope a were obtained.

References

[1] Dominic Greiffenberg, Marie Andrä, Rebecca Barten, Anna Bergamaschi, Martin Brückner, Paolo Busca, Sabina Chiriotti, Ivan Chsherbakov, Roberto Dinapoli, Pablo Fajardo, Erik Fröjdh, Shqipe Hasanaj, Pawel Kozlowski, Carlos Lopez Cuenca, Anastassiya Lozinskaya, Markus Meyer, Davide Mezza, Aldo Mozzanica, Sophie Redford, Marie Ruat, Christian Ruder, Bernd Schmitt, Dhanya Thattil, Gemma Tinti, Oleg Tolbanov, Anton Tyazhev, Seraphin Vetter, Andrei Zarubin, Jiaguo Zhang, Characterization of Chromium compensated GaAs sensors with the charge-integrating JUNGFRAU readout chip by means of a highly collimated pencil beam, Sensors 21 (4) (2021) 1550, http://dx.doi.org/10.3390/s21041550.

[2] C. Ponchut, M. Cotte, A. Lozinskaya, A. Zarubin, O. Tolbanov, A. Tyazhev, Characterisation of GaAs:Cr pixel sensors coupled to timepix chips in view of synchrotron applications, J. Instrum. 12 (12) (2017) C12023, http://dx.doi.org/10.1088/1748-0221/12/12/C12023.

[3] M. Ruat, C. Ponchut, Defect signature, instabilities and polarization in CdTe x-ray sensors with quasi-ohmic contacts, J. Instrum. 9 (04) (2014) C04030, http://dx.doi.org/10.1088/1748-0221/9/04/C04030.

[4] Stefano Del Sordo, Leonardo Abbene, Ezio Caroli, Anna Maria Mancini, Andrea Zappettini, Pietro Ubertini, Progress in the development of CdTe and CdZnTe semiconductor radiation detectors for astrophysical and medical applications, Sensors (Basel) 9 (5) (2009) 3491–3526, http://dx.doi.org/10.3390/s90503491.

[5] Derek S. Bale, Csaba Szeles, Nature of polarization in wide-bandgap semiconductor detectors under high-flux irradiation: application to semi-insulating $Cd_{1-x}Zn_xTe$, Phys. Rev. B 77 (2008) 035205, http://dx.doi.org/10.1103/PhysRevB.77.035205.

[6] K. Iniewski, CZT detector technology for medical imaging, J. Instrum. 9 (11) (2014) C11001, http://dx.doi.org/10.1088/1748-0221/9/11/C11001.

[7] B. Thomas, M.C. Veale, M.D. Wilson, P. Seller, A. Schneider, K. Iniewski, Characterisation of redlen high-flux CdZnTe, J. Instrum. 12 (12) (2017) C12045, http://dx.doi.org/10.1088/1748-0221/12/12/C12045.

[8] M.C. Veale, C. Angelsen, P. Booker, J. Coughlan, M.J. French, A. Hardie, M. Hart, J. Lipp, T. Nicholls, A. Schneider, P. Seller, D. Sole, B. Thomas, M. Wilson, G.A. Carini, P. Hart, K. Nakahara, T. Sato, C. Hansson, K. Iniewski, P. Marthandam, G. Prekas, Cadmium Zinc Telluride pixel detectors for high-intensity X-ray imaging at free electron lasers, J. Phys. D: Appl. Phys. 52 (8) (2018) 085106, http://dx.doi.org/10.1088/1361-6463/aaf556.

[9] O. Baussens, C. Ponchut, M. Ruat, M. Bettelli, S. Zanettini, A. Zappettini, Characterization of high-flux CdZnTe with optimized electrodes for 4th generation synchrotrons, J. Instrum. 17 (11) (2022) C11008, http://dx.doi.org/10.1088/1748-0221/17/11/C11008.

[10] B.D. Cline, D. Banks, S. Bell, I. Church, A. Davis, T. Gardiner, J. Harris, M. Hart, L. Jones, T. Nicholls, J. Nobes, S. Pradeep, M. Roberts, D. Sole, M.C. Veale, M.D. Wilson, V. Dhamgaye, O. Fox, K. Sawhney, Characterisation of redlen HF-CdZnTe at $> 10^6 phs^{-1} mm^{-2}$ using $HEXITEC_{MHz}$, J. Instrum. 19 (04) (2024) P04028, http://dx.doi.org/10.1088/1748-0221/19/04/P04028.

[11] Manuele Bettelli, Silvia Zanettini, Leonardo Abbene, Francesca Casoli, Lucia Nasi, Giovanna Trevisi, Fabio Principato, Antonino Buttacavoli, Andrea Zappettini, High performance platinum contacts on high-flux CdZnTe detectors, Sci. Rep. (ISSN: 2045-2322) 13 (1) (2023) 17963, http://dx.doi.org/10.1038/s41598-023-45331-9.

[12] Adriano Cola, Isabella Farella, The polarization mechanism in CdTe schottky detectors, Appl. Phys. Lett. (ISSN: 0003-6951) 94 (10) (2009) 102113, http://dx.doi.org/10.1063/1.3099051.

[13] Aschkan Allahgholi, Julian Becker, Annette Delfs, Roberto Dinapoli, Peter Goettlicher, Dominic Greiffenberg, Beat Henrich, Helmut Hirsemann, Manuela Kuhn, Robert Klanner, Alexander Klyuev, Hans Krueger, Sabine Lange, Torsten Laurus, Alessandro Marras, Davide Mezza, Aldo Mozzanica, Magdalena Niemann, Jennifer Poehlsen, Joern Schwandt, Igor Sheviakov, Xintian Shi, Sergej Smoljanin, Lothar Steffen, Jolanta Sztuk-Dambietz, Ulrich Trunk, Qingqing Xia, Mourad Zeribi, Jiaguo Zhang, Manfred Zimmer, Bernd Schmitt, Heinz Graafsma, The adaptive gain integrating pixel detector at the European XFEL, J. Synchrotron Radiat. 26 (1) (2019) 74–82, http://dx.doi.org/10.1107/S1600577518016077.

[14] D. Magalhaes, H. Hirsemann, A. Klujev, Z. Konopkova, S. Lange, T. Laurus, M. Niemann, S. Palutke, D. Pennicard, M. Ramilli, V. Rovensky, C. Strohm, J. Sztuk-Dambietz, U. Trunk, M. Veale, M. Wilson, H. Graafsma, High-Z sensors at MHz repetition rate FELs: first AGIPD results, J. Instrum. 21 (01) (2026) C01019, http://dx.doi.org/10.1088/1748-0221/21/01/C01019.

[15] J. Becker, Signal Development in Silicon Sensors Used for Radiation Detection. Dr., Hamburg University, Hamburg, 2010, Hamburg University. Diss. 2010.

[16] Finn Feindt, Edge-TCT for the Investigation of Radiation Damaged Silicon Strip Sensors, Ms, Universität Hamburg, Hamburg, 2017, Universität Hamburg, Masterarbeit, 2016.

[17] PicoQuant GmbH, https://www.picoquant.com/. (Accessed 28 July 2026).

[18] Emil Kamieniecki, Effect of defect clusters on carrier recombination in high-resistivity CdZnTe, J. Appl. Phys. (ISSN: 0021-8979) 114 (19) (2013) 193701, http://dx.doi.org/10.1063/1.4831954.

[19] DESY, Machine parameters PETRA III (design values), 2026, https://photon-science.desy.de/facilities/petra_iii/machine/parameters/index_eng.html. (Accessed 04 June 2026).

[20] A.M. Abousehly, H.M. Abu basha, A.A. El-sharkawy, Thermophysical properties and mechanism of heat transfer of polycrystalline CdS, CdSe, and CdTe in the temperature range 300–700 K, High Temp. High Press. (Print) (ISSN: 0018-1544) (1990).

[21] S. Carslaw Horatio, John C. Jaeger, Conduction of Heat in Solids, second ed., Oxford University Press, Oxford, 1959.

[22] Andrey Tselin, Mariia Pogodaeva, Sergey Levchenko, Aleksey Kalmykov, Konstantin Garbuzov, Alexander Smirnov, Vladimir Drachev, Exploring the dielectric function of platinum, Phys. Rev. B 110 (2024) 195130, http://dx.doi.org/10.1103/PhysRevB.110.195130.

[23] M. Betušiak, P. Praus, R. Grill, E. Belas, J. Pipek, A.E. Bolotnikov, R.B. James, Large-volume CdZnTe bar detectors characterized by laser-induced transient currents, J. Appl. Phys. (ISSN: 0021-8979) 134 (22) (2023) 224501, http://dx.doi.org/10.1063/5.0160766.

[24] Adriano Cola, Isabella Farella, Marco Anni, Charge transients by variable wavelength optical pulses in CdTe nuclear detectors, in: 2011 IEEE Nuclear Science Symposium Conference Record, Valencia, Spain, IEEE, 2011, pp. 4604–4610, http://dx.doi.org/10.1109/nssmic.2011.6154743.

[25] M. Hellwig, T. Kuhwald, Advanced signal analysis using the history mode of the R&S®RTO oscilloscope, 2026, Rohde & Schwarz Application Note 1TD02_0e. https://scdn.rohde-schwarz.com/ur/pws/dl_downloads/dl_application/application_notes/1td02/1TD02_0e_RTO_History_Mode.pdf. (Accessed 24 September 2026).

[26] M. Niraula, A. Nakamura, T. Aoki, Y. Tomita, Y. Hatanaka, Stability issues of high-energy resolution diode type CdTe nuclear radiation detectors in a long-term operation, Nucl. Instrum. Methods Phys. Res. Sect. A: Accel. Spectrometers Detect. Assoc. Equip. (ISSN: 0168-9002) 491 (1) (2002) 168–175, http://dx.doi.org/10.1016/S0168-9002(02)01175-0.

[27] A. Many, High-field effects in photoconducting cadmium sulphide, J. Phys. Chem. Solids (ISSN: 0022-3697) 26 (3) (1965) 575–578, http://dx.doi.org/10.1016/0022-3697(65)90133-2.

[28] A. Santi, M. Zanichelli, G. Piacentini, M. Pavesi, A. Cola, I. Farella, An original method to evaluate the transport parameters and reconstruct the electric field in solid-state photodetectors, Appl. Phys. Lett. (ISSN: 0003-6951) 104 (19) (2014) 193503, http://dx.doi.org/10.1063/1.4876178.

[29] J. Fink, H. Krüger, P. Lodomez, N. Wermes, Characterization of charge collection in CdTe and CZT using the transient current technique, Nucl. Instrum. Methods Phys. Res. Sect. A: Accel. Spectrometers Detect. Assoc. Equip. (ISSN: 0168-9002) 560 (2) (2006) 435–443, http://dx.doi.org/10.1016/j.nima.2006.01.072.

[30] Stepan Uxa, Eduard Belas, Roman Grill, Petr Praus, Ralph B. James, Determination of electric-field profile in CdTe and CdZnTe detectors using transient-current technique, IEEE Trans. Nucl. Sci. 59 (5) (2012) 2402–2408, http://dx.doi.org/10.1109/TNS.2012.2211615.

[31] M. Martini, J.W. Mayer, K.R. Zanio, Drift velocity and trapping in semiconductors—transient charge technique, in: Raymond Wolfe, in: Applied Solid State Science, vol. 3, Elsevier, 1972, pp. 181–261, http://dx.doi.org/10.1016/B978-0-12-002903-7.50010-2.

[32] Aleksey E. Bolotnikov, Steven E. Boggs, C.M. Hubert Chen, Walter R. Cook, Fiona A. Harrison, Stephen M. Schindler, Properties of Pt Schottky type contacts on high-resistivity CdZnTe detectors, Nucl. Instrum. Methods Phys. Res. Sect. A: Accel. Spectrometers Detect. Assoc. Equip. (ISSN: 0168-9002) 482 (1) (2002) 395–407, http://dx.doi.org/10.1016/S0168-9002(01)01506-6.

[33] Gangqiang Zha, Wanqi Jie, Tingting Tan, Wenhua Zhang, Faqiang Xu, The interface reaction and schottky barrier between metals and CdZnTe, J. Phys. Chem. C 111 (34) (2007) 12834–12838, http://dx.doi.org/10.1021/jp0734070.

[34] M. Bishop, M.C. Veale, S.L. Bugby, F.K. Dejene, M. Bettelli, S. Zanettini, Comparison of the charge transport properties of low and high flux grade Redlen CdZnTe crystals, J. Instrum. 20 (09) (2025) P09009, http://dx.doi.org/10.1088/1748-0221/20/09/P09009.

[35] J.H. Hubbell, S.M. Seltzer, Tables of x-ray mass attenuation coefficients and mass energy-absorption coefficients (version 1.4), 1995, http://physics.nist.gov/xaamdi. (Accessed 14 July 2026).